Agricultural and Forest Meteorology 232 (2017) 606–622

Contents lists available at ScienceDirect

Agricultural and Forest Meteorology

journal homepage: www.elsevier.com/locate/agrformet

Using the particle swarm optimization algorithm to calibrate the parameters relating to the turbulent flux in the surface layer in the source region of the Yellow River

Qidong Yang[a,*], Jian Wu[a], Yueqing Li[b], Weidong Li[a], Lijuan Wang[c], Yang Yang[c]

[a] Department of Atmospheric Sciences, Yunnan University, Yunnan Province 650091, China
[b] Institute of Plateau Meteorology, China Meteorological Administration, Sichuan Province 610000, China
[c] Gansu Key Laboratory of Arid Climatic Change and Reducing Disater/Key Open Laboratory of Arid Climatic Change and Disaster Reduction of CMA, Institute of Arid Meteorology, China Meteorological Administration, Gansu Province 730020, China

ARTICLE INFO

Article history:
Received 10 March 2016
Received in revised form 18 October 2016
Accepted 24 October 2016
Available online 28 October 2016

Keywords:
Maqu station
Monin-Obukhov similarity theory
Particle swarm optimization algorithm
Source region of the Yellow River

ABSTRACT

Accurately determining the fluxes of mass and energy between land and the atmosphere is important for understanding regional climates and hydrological cycles. In numerical modeling, the parameterization of a turbulent flux is usually based on Monin-Obukhov similarity theory (MOST). According to this theory, it is necessary to simultaneously calculate the empirical similarity parameters β_m, β_h, γ_m, and γ_h, the aerodynamic roughness (z_{0m}) and the thermal roughness (z_T). However, it is difficult to solve a simultaneous set of nonlinear equations for these six parameters. In this study, a new method was introduced to solving this problem. Using measurements from Maqu Station in the source region of the Yellow River, this study employed the artificial intelligence particle swarm optimization (PSO) algorithm to calibrate the parameters relating to the turbulent flux in the surface layer. We concluded that the differences in the sensible heat and momentum fluxes between the calculations that used the calibrated parameters and the measurements were rather small and that their correlation coefficients were relatively high. The results suggested that PSO algorithm is a feasible approach which can be applied in MOST parameter estimation.

1. Introduction

The atmospheric surface layer is at the bottom of the atmospheric boundary layer. Due to the strong aerodynamic and thermal effects of the underlying surface, atmospheric motion is dominated by turbulence. The mass and energy exchanges that occur between the atmosphere and land surface via turbulent fluxes significantly impact both weather and climate (Dickinson et al., 1998; Seneviratne et al., 2006). In numerical modeling, schemes for parameterizing the turbulent surface flux enforce the balances of mass and energy between land and the atmosphere (Beljaars and Holtslag, 1991; Chen et al., 1997; Garratt and Pielke, 1989). Therefore, to improve the performance of climate models, it is important to carefully study the physical interactions between different types of land surface and the atmosphere, develop optimal schemes for parameterizing the turbulent fluxes and accurately determine the land-atmosphere fluxes of mass and energy.

In global climate models, the land-atmosphere fluxes of momentum, sensible heat and water vapor are usually calculated using the wind velocity, potential temperature and humidity gradients with the relevant bulk transfer coefficients (Dai, 2003; Niu, 2011; Zeng and Dickinson, 1998). The wind velocity, potential temperature and humidity gradients can be directly measured. Therefore, accurately determining the bulk transfer coefficients is the key to parameterizing the turbulent fluxes in numerical models. Since the Monin-Obukhov similarity theory (MOST) was proposed in the 1950s (Dyer, 1974; Monin and Obukhov, 1954), significant breakthroughs have been made in the parameterization of surface turbulent fluxes (Businger et al., 1971; Dyer, 1974). More than 20 parameterization schemes for the bulk transfer coefficients have been developed based on this theory (Abdella and McFarlane, 1996; Łobocki, 1993; Louis, 1979; Paulson, 1970), and these schemes have been widely applied in various types of numerical model. Accord-

* Corresponding author.
E-mail address: yangqd@ynu.edu.cn (Q. Yang).

http://dx.doi.org/10.1016/j.agrformet.2016.10.019

ing to MOST, the land-atmosphere bulk transfer coefficients can be represented as follows:

$$C_D = \frac{\kappa^2}{\left[\ln(z/z_{0m}) - \psi_m(z/L)\right]^2} \quad (1)$$

$$C_H = C_E = \frac{\kappa^2}{\left[\ln(z/z_{0m}) - \psi_m(z/L)\right]\left[\ln(z/z_T) - \psi_h(z/L)\right]} \quad (2)$$

where C_D, C_H and C_E are the bulk transfer coefficients of momentum, sensible heat and water vapor, respectively, κ is the von Karman constant. Ψ_M and Ψ_H are the integrals of the similarity functions associated with momentum and heat. z is a reference height, L is the Obukhov length, z/L represents the atmospheric stability, z_{0m} is the aerodynamic roughness and z_T is the thermal roughness.

Many studies of the similarity functions in the above equations have been conducted (Businger et al., 1971; Dyer, 1974; Högström, 1996). Near-surface measurements with different underlying surface types were found to lead to different forms of these functions (van den Hurk and Holtslag, 1997). Sorbjan (1986) reviewed previous results and summarized the similarity functions for the momentum and sensible heat as follows, based on the status of the atmospheric stability (Sorbjan, 1986):

$$\phi_m = \begin{cases} 1 + \beta_m(\frac{z}{L})\frac{z}{L} \geq 0 \\ -1/4\frac{z}{L} < 0 \end{cases} \quad (3)$$

$$\phi_h = \begin{cases} 1 + \beta_h\frac{z}{L}\frac{z}{L} \geq 0 \\ -1/2\frac{z}{L} < 0 \end{cases} \quad (4)$$

where φ_m and φ_h are the differential expressions of the similarity functions, β_m and β_h, and γ_m and γ_h are empirical parameters that are normally regressed from measurements. In numerical models, the similarity functions obtained by Businger and Dyer have been most widely used (Dai, 2003; Niu, 2011; Oleson et al., 2010). In these functions, the empirical parameters are $\beta_m = \beta_h = 16$ and $\gamma_m = \gamma_h = 4.7$. However, these functions are not always suitable for all seasons and surface types. Numerous studies have shown that the selection of empirical parameters depends largely on the physical properties of the underlying surface, the accuracy of the measurements and the methods of the study (Högström, 1988).

The stability parameter z/L determines the atmosphere's motion and thermal status. It is usually an implicit function of C Yang et al. (2001) suggested that z/L can be represented by the bulk Richardson number and similarity functions (Yang et al., 2001). Under stable conditions, because the similarity functions are linear, an analytical solution for z/L is available. In contrast, under unstable conditions, the similarity functions are nonlinear, and z/L can be obtained via iteration or semi-analytical methods (Abdella and McFarlane, 1996; Łobocki, 1993; Louis, 1979; Paulson, 1970; Sharan and Srivastava, 2014). The atmosphere aerodynamic and thermal roughness lengths are two parameters that are important for calculating the bulk transfer coefficients. They represent the heights at which the surface wind velocity reaches zero and at which the surface temperature is equal to the atmospheric temperature. These two parameters are difficult to measure directly; therefore, they are often taken as empirical parameters in near-surface studies (Kanda et al., 2007; MacKinnon et al., 2004). Present studies suggest that the aerodynamic roughness strongly depends on the surface conditions. Therefore, in land surface models (i.e. CLM, NOAH), the underlying surface is divided into different types, and each type is assigned a different aerodynamic roughness (Oleson et al., 2010). Thermal roughness was originally considered identical to aerodynamic roughness (Louis, 1979), but further development in near-surface measurements and research have shown that thermal roughness is normally less than aerodynamic roughness (Sun, 1999; Yang et al., 2008, 2003). We can use $KB^{-1} = \ln(z_{0m}/z_T)$ to compare the two parameters. Accurately determining the aerodynamic and thermal roughnesses or KB^{-1} is critical for improving the parameterization of the turbulent flux.

From the above analysis and a combination of Eqs. (1) and (2), we can see that C_D depends on β_m, γ_m and z_{0m} and that C_H depends on β_m, β_h, γ_m, γ_h, z_{0m} and z_T. Together, these six parameters affect the bulk transfer coefficients, which can be obtained after simultaneously solving for β_m, β_h, γ_m, γ_h, z_{0m} and z_T. Determining these six parameters simultaneously requires solving a set of non-linear equations. The calculation is complex, iterative and time consuming. Previous conventional studies usually selected similarity functions, that is, assigned a value to β_m, β_h, γ_m, γ_h, and then calculated the others using the multi-layer wind velocity and potential temperature profiles under neutral conditions. Then, the bulk transfer coefficients could be calculated. This method suffered from a few pitfalls: (1) It reduced the six parameters in the original parameterization scheme to one or two parameters and did not verify the suitability of the similarity functions and the sensitivity of the calculation. (2) The six parameters were mutually related. Calculating z_{0m} or z_T using profiles of the wind velocity and the potential temperature may accurately yield one of the two bulk transfer coefficients for the momentum or sensible heat but cannot accurately yield both. (3) An accurate calculation of z_{0m} or z_T requires accurate profiles of the multi-layer wind velocity and the potential temperature. In addition, different neutral condition ranges could lead to large variations in the results. Therefore, it is necessary to investigate methods of efficiently calculating the turbulent flux parameters that avoid the caveats of the conventional approach.

The recent development of the particle swarm optimization (PSO) algorithm used in artificial intelligence provides one possible method for solving the above problem (Kennedy and Eberhart, 1995; Poli et al., 2007). This algorithm mimics animal activities such as the process birds and fish use for finding food, which essentially is a particle constrained by a certain object function solving a global or quasi-global optimal solution within a given space. Therefore, many studies have used this method to calibrate the parameters of continental hydrological models. For example, Gill et al. used a multi-objective particle swarm algorithm to estimate hydrological parameters (Gill et al., 2006). Chau et al. combined the PSO algorithm with artificial neural networks (ANNs) to predict water levels (Chau, 2006). Scheerlinck et al. used the PSO algorithm to calibrate the parameters of a simple hydrological model and found that it was easy to implement and used measurements efficiently (Scheerlinck et al., 2009).

Calibrating the turbulent flux parameters is a similar optimization process; i.e., given a different parameter space, we compare the errors between the calculated and measured values of the momentum and sensible heat fluxes within a time period, evaluate the suitability of the parameters and then obtain more accurate parameters. Hence, many optimization algorithm can be used to calibrate the turbulent flux parameters. Compared with other algorithm, the PSO algorithm has the following advantages to calibrate the surface-layer turbulent flux. (1) The particle swarm optimization is easy to implement with a set of non-linear equations to find the optimum solution. Furthermore, according to the theoretical study of PSO algorithm, it was proved that the PSO algorithm can get approximate global optimum, and has a lesser tendency of getting trapped in local minima (Schmitt and Wanka, 2015). The optimum solution is not affected by the velocity, iteration number, and initial value. (2) The ranges of turbulent fluxes related parameters have been able to obtain, but the exact values is still difficult to determine

because these parameters have temporal and spatial variations. The PSO algorithm can be used to find optimal solution for a given parameter space. (3) We can easily define an objective function in PSO algorithm by observed and calculated turbulent fluxes. In view of above-mentioned reasons, this study attempts to introduce the PSO algorithm to calibrate the surface layer parameters, and then accurately determine the momentum and heat flux between the land and atmosphere.

This study used the data from Maqu Station located in source region of the Yellow River, and employd the particle swarm algorithm to calibrate the surface layer parameters.Then the sensible heat and momentum fluxes were calculated using the calibrated parameters. The study was benefit for providing reliable parameters in future numerical modeling, and, in turn, to improve the performance of models used for simulating the climate of this region.

2. Data

The data used in this study were from Maqu Climate and Environment Comprehensive Observation Station (33°52′N, 102°09′E, 3443 m in altitude), which was established by the Cold and Arid Regions Environmental and Engineering Research Institute (CAREERI) of the Chinese Academy of Sciences. Maqu Station is located in the source region of the Yellow River (95°50′–103°30′E, 32°30′–36°05′N) which is a part of the Tibetan Plateau. The land surface types of this region are alpine meadow, permafrost, and snow (Cuo et al., 2013). Surface runoff accounts for approximately one third of the total discharge of the Yellow River. In recent years, the temperature of this region has been gradually increasing, which has caused the permafrost to retreat and thus changed the land-atmosphere fluxes of mass and energy (Fu et al., 2004; Hu et al., 2012). These changes could further lead to systematic changes in the regional climate, ecology, and water resources. Accordingly. the CAREERI established Maqu Station to study climate change in this region. The Maqu Station has made measurements over two years and provided a sound basis for studying the land-atmosphere interactions in this region.

The position of the Maqu Station is shown in Fig. 1(a). During 2009–2011, the annual mean air temperature is 275 K, the annual mean wind speed is 2.5 m s^{-1}, and the annual total precipitation is 420 mm. More than two-thirds of the annual precipitation is occurred in the summer and autumn. The land surface of Maqu station is flat without any mountains, large scale terrain (Fig. 1b). The underlying cover is dominated by alpine plants, including the Kobresia tibetica, Potentilla anserine, Kobresia humilis etc. The total vegetation coverage is about 92%. In winter and spring season the average plant height is about 5 cm. With the increase of precipitation, the short grass begins to grow in May. In summer and autumn season the mean plant height can up to 15 cm. In the 0–20 cm depth, the sand, clay and silt content is about 25%, 70%, and 5%. Maqu Station can represent the climate condition within a few hundreds of kilometers in the source region of the Yellow River.

Maqu Station is equipped with a micro-meteorological tower, an ultrasonic detector, a radiation sensor, a soil temperature and moisture system and other equipment, which enable it to record the near-surface wind velocity, wind direction, pressure, amount of radiation and turbulent flux. The details are listed in Table 1. Maqu Station has joined the Chinese Terrestrial Ecosystem Flux Research Network (ChinaFLUX), from which data have been widely used in atmospheric and hydrological studies.

This study used half-hourly data of the wind velocity (u), air temperature (T_a), and relative humidity (h) at the reference height at 7.17 m, atmospheric pressure (p), surface temperature (T_s), sensible heat flux (H) and momentum flux (τ) collected at Maqu Station between July 2009 and July 2011. Data quality control was performed using the following criteria:

$$|T_a| < 50^{o}\mathrm{C}, |T_s| < 100^{o}\mathrm{C}, 0.01\mathrm{ms}^{-1} < u < 20\mathrm{ms}^{-1}\ \ 0.01\mathrm{kg\,m}^{-1}\mathrm{s}^{-2} < \tau < 2.0\mathrm{kg\,m}^{-1}\mathrm{s}^{-2},\ \ H > -30\mathrm{Wm}^{-2}.$$

After completing the quality control process and removing the missing data, we found that the data from October, November and December of 2009 and 2011 were completely unusable, whereas only a few of the data points from other months were removed. Accordingly, we divided the available data into two groups further referred to as the C1 and C2 period. The C1 period, contained data collected between July 2009 and June 2010, and the C2 period, contained data collected between July 2010 and June 2011.We use data in both periods to calibrate parameters every month, because the variation of these parameters is little in month scale. The C1 is used as training data set whereas the C2 is then used as validation data set, or vice versa. In short, V1, the C1 validation period corresponds to the C2 calibration period, and V2, the C2 validation period corresponds to C1 calibration period.

3. Methods

3.1. Turbulent fluxes parameterization schemes

In the numerical model, the following formulas were used to calculate the land-atmosphere fluxes of momentum, sensible heat and water vapor, respectively:

$$\tau = \rho C_D (u - u_s)^2 \tag{5}$$

$$H = \rho C_p C_H (u - u_s)(\theta_s - \theta) \tag{6}$$

$$E = \rho C_E (u - u_s)(q_s - q) \tag{7}$$

where τ, H and E are the fluxes of momentum, sensible heat and water vapor, respectively, C_D, C_H and C_E are the bulk transfer coefficients of momentum, sensible heat and water vapor, ρ and C_p are the air density and specific heat, respectively, u (u_s), θ (θ_s) and q (q_s) are the (land surface) wind velocity, potential temperature and specific humidity at 7.17m, respectively, and $u_s = 0$ at the height of the roughness length. The turbulent fluxes between the land and atmosphere can be calculated using the parameterization of C_D, C_H and C_E. Due to the difficulty of measuring the specific humidity at the land surface, we only examined the momentum and sensible heat fluxes between the land and atmosphere.

According to MOST, the dimensionless wind velocity, potential temperature and specific humidity gradients can be written as follows:

$$\frac{\kappa z}{u_*}\frac{\partial u}{\partial z} = \phi_m\left(\frac{z}{L}\right) \tag{8}$$

$$\frac{\kappa z}{\theta_*}\frac{\partial \theta}{\partial z} = \phi_h\left(\frac{z}{L}\right) \tag{9}$$

where κ is the von Karman constant, u_* and θ_* are the friction velocity, the characteristic potential temperature, respectively. Integrating the above gradients results in the following equations:

$$u = \frac{u_*}{\kappa}\left[\ln\left(\frac{z}{z_{0m}}\right) - \psi_m\left(\frac{z}{L}\right)\right] \tag{10}$$

and

$$\theta - \theta_s = \frac{\theta_*}{\kappa}\left[\ln\left(\frac{z}{z_T}\right) - \psi_h\left(\frac{z}{L}\right)\right] \tag{11}$$

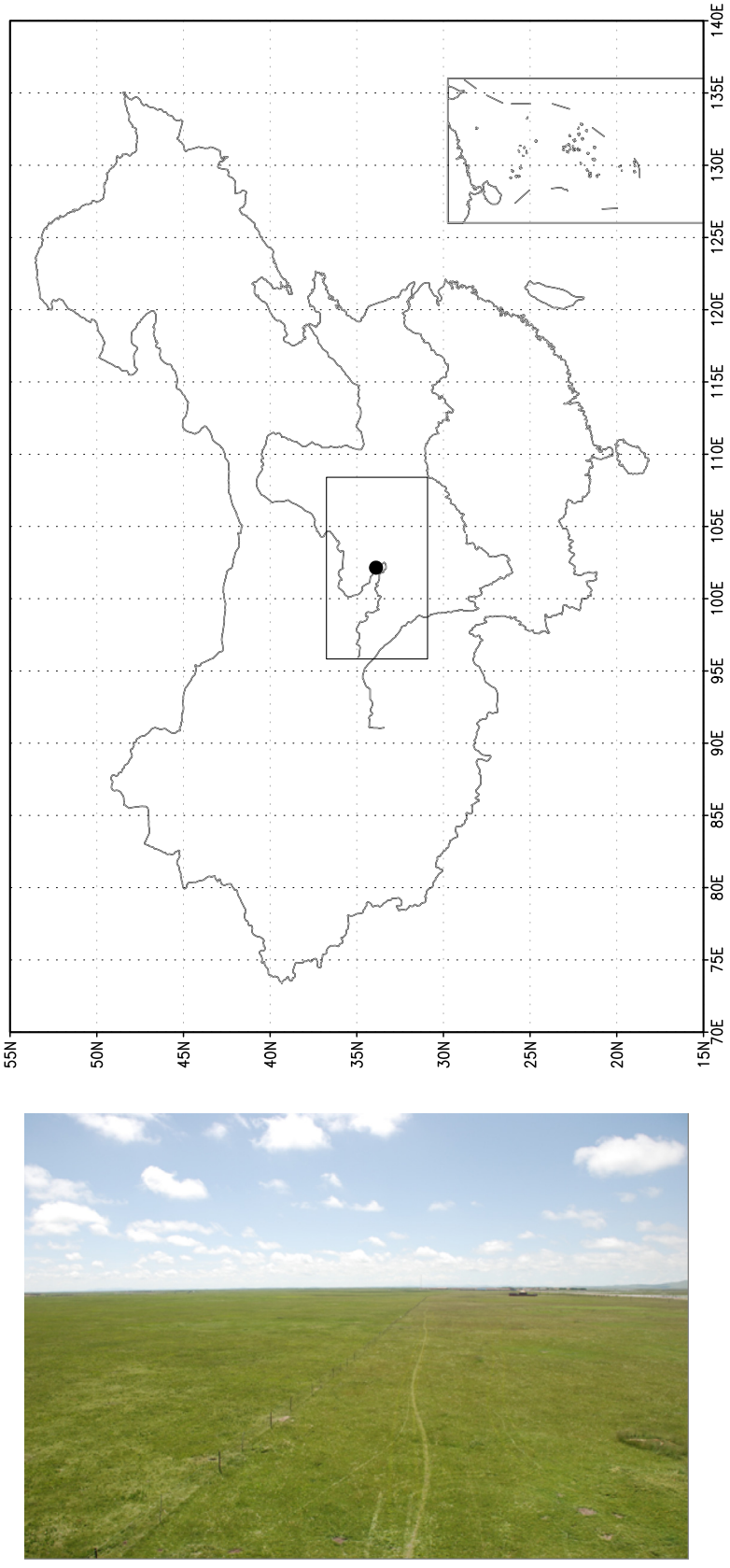

Fig. 1. (a) The location of Maqu Station (b) the underlying cover of Maqu Station.

Table 1
The observational variables and sensors of Maqu Station.

Variables	Height	Type of sensors
Wind speed	2.35,4.20,7.17,10.13,18.15 m	Windsonic by Gill
Air temperature and humidity	2.35,4.20,7.17,10.13,18.15 m	HMP45C21 by Vaisalla
Wind direction	10.8 m	W200P of Vector
Radiation	2 m	CNR1 by Kipp&Zonen
Sensible heat flux	3.2 m	CSAT3 by Campbell
Carbon and water flux	3.2 m	LI7500, LI-COR by Campbell
Precipitation	–	T200B by Geonor
Soil temperatue	−5,−10,−20,−80,−160 cm	107L by Campbell
Soil moisture	−5,−10,−20,−80,−160 cm	CS616 by Campbell

and where (Yang et al., 2008)

$$\psi_m = \begin{cases} -\beta_m \dfrac{(z - z_{0m})}{L} & \dfrac{z}{L} \geq 0 \\ 2\ln(\dfrac{1+x}{1+x_0}) + \ln(\dfrac{1+x^2}{1+x_0^2}) - 2\tan^{-1}x + 2\tan^{-1}x_0 & \dfrac{z}{L} < 0 \end{cases} \quad (12)$$

and

$$\psi_h = \begin{cases} -\beta_h \dfrac{(z - z_{0m})}{L} & \dfrac{z}{L} \geq 0 \\ 2\ln(\dfrac{1+y}{1+y_0}) & \dfrac{z}{L} < 0 \end{cases} \quad (13)$$

where

$$x = (1 - \gamma_m z/L)^{1/4},\ x_0 = (1 - \gamma_m z_{0m}/L)^{1/4} \quad (14)$$

$$y = (1 - \gamma_h z/L)^{1/2}, y_0 = (1 - \gamma_h z_T/L)^{1/2} \quad (15)$$

The profiles of the wind velocity, potential temperature and specific humidity can be used to derive the bulk transfer coefficients in Eqs. (1) and (2). Therefore,

$$C_D = C_D(\beta_m, \gamma_m, z_{0m}) \quad (16)$$

$$C_H = C_H(\beta_m, \beta_h, \gamma_m, \gamma_h, z_{0m}, z_T) \quad (17)$$

Simultaneously determining β_m, β_h, γ_m, γ_h, z_{0m}, z_T or (KB^{-1}) allows these equations to be used to calculate the bulk transfer coefficients. In combination with the measured wind velocity and the air and surface temperatures, these coefficients can be used to calculate the turbulent fluxes.

3.2. PSO algorithm

The PSO algorithm was first introduced by Kennedy and Eberhart (1995) to simulate the society physiological behavior and was later expanded to other applications and became an optimization method to solve the global optimal solution for large-scale non-linear problems (Kennedy and Eberhart, 1995). The principle of PSO is to assign coordinates and initial velocities for a group of randomly chosen particles and then search the position in the space within a defined region. By continuously updating the positions and velocities of these particles, the algorithm compares the object function of each particle to obtain the local optimal position and finally the global optimal position.

If we want to optimize an n-dimensional problem for m particles, the position and velocity vector of the i^{th} ($i = 1,2,\ldots,m$) particle can be expressed as:

$$\mathbf{x}_i = (x_{i1}, x_{i2}, \ldots, x_{in}) \quad (18)$$

$$\mathbf{v}_i = (v_{i1}, v_{i2}, \ldots, v_{in}) \quad (19)$$

The updated position and velocity of the i^{th} particle can be expressed as:

$$\mathbf{v}_{in}^{N+1} = \omega \mathbf{v}_{in}^{N} + c_1 r_1 (\mathbf{p}_{in}^{N} - \mathbf{x}_{in}^{N}) + c_2 r_2 (\mathbf{G}_{n}^{N} - \mathbf{x}_{in}^{N}) \quad (20)$$

$$\mathbf{x}_{in}^{N+1} = \mathbf{x}_{in}^{N} - \mathbf{v}_{in}^{N} \quad (21)$$

in which N represents the number of iterations; ω represents the inertia weight; c_1 and c_2 are the acceleration constants, which are the weight coefficients of the optimal value by tracking its own history and therefore represent self-awareness of the particle; r_1 and r_2 are random numbers in [0,1]. $\boldsymbol{p}_i$ and $\boldsymbol{G}_n$ represent the optimal value of the i^{th} particle by looking into the historic global optimum record and the current optimal position among all the particles, respectively, which can be expressed as:

$$\mathbf{p}_i = (p_{i1}, p_{i2}, \ldots, p_{in}) \quad (22)$$

$$\mathbf{G}_n = (p_{g1}, p_{g2}, \ldots, p_{gn}) \quad (23)$$

$$g = \min_{1 \leq i \leq n} [\mathbf{f}(\mathbf{p}_i)] \quad (24)$$

in which g represents the position when the value of the object function is the lowest and $\mathbf{f}$ is the object function. The object function $\mathbf{f}$ in the PSO algorithm can be a single function or vector function. When $\mathbf{f}$ is a vector function, it should be the multiple object function; therefore, one method is to solve for its Pareto front (Gupta et al., 1999), and another method, proposed by Crow et al. (2003) is to standardize multiple variables with different orders of magnitude and then define a single object function to solve for its minimum (Crow et al., 2003).

3.3. Calibration method

When utilizing the PSO algorithm to calibrate parameters, an object function must be defined. In this study, the Kling-Gupta efficiency (KGE) function proposed by Gupta et al. (2009) is used as the object function, which is defined as (Gupta et al., 2009):

$$KGE = 1 - \sqrt{(r-1)^2 + (\alpha - 1)^2 + (\beta - 1)^2} \quad (25)$$

in which r represents the correlation coefficient between the observational and calculation value, α represents the ratio of the standard deviation of the observational value to that of the calculation value, and β represents the ratio of the mean observational value to the mean calculation value. KGE is used to evaluate the quality of the fit for the calculation result with the observation, whose range varies from $-\infty$ to 1; the closer the value is to 1, the better the calculation capability. The KGE_j (j specifies the momentum and sensible heat flux) are calculated using momentum and sensible heat flux with corresponding calculated and observed values. The final KGE is the average of all KGE_j values. Because the momentum and sensible heat fluxes have different orders of magnitude, they are standardized during the calculation, i.e., the average value is subtracted from each observational or calculation value, which is then divided by the corresponding standard deviation.

The PSO algorithm also depends on parameters of the model itself, specifically, the number of particles, and the position and velocity variation range of each particle, etc. According to multiple tests and previous studies (Scheerlinck et al., 2009), (1) $m = 30$; (2)

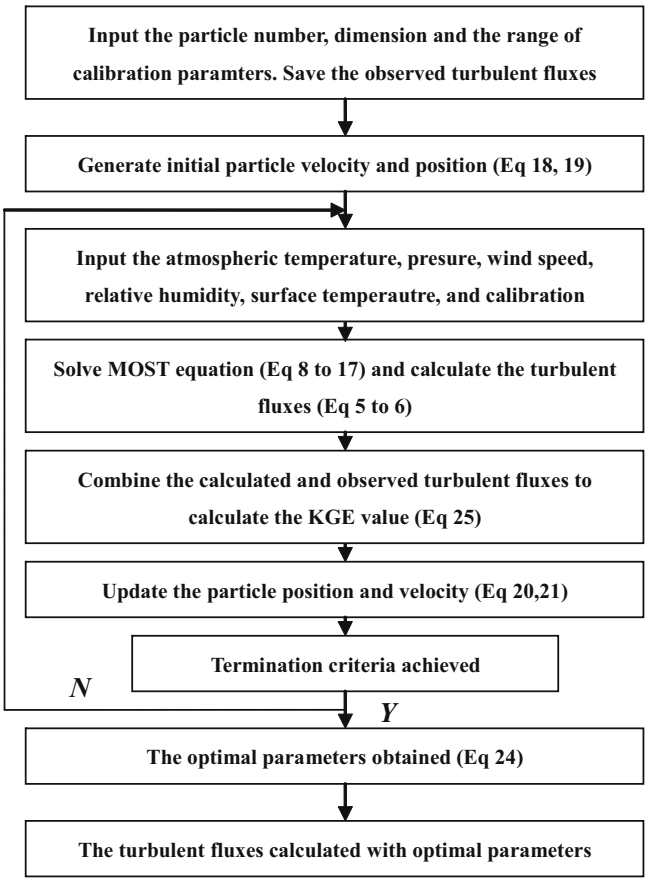

Fig. 2. The combination of turbulent flux parameterization schemes and PSO algorithm.

$N = 200$; (3) the variation range of w is from 0.2 to 0.5; (4) $c_1 = 1.8$, and $c_2 = 2.0$; (5) the variation range of the particle position is from -1 to 1, and that of the particle velocity is from -0.01 to 0.01. For all parameters that must be calibrated, their variation ranges become $[-1, 1]$ by the following method:

$$\mathbf{x} = \frac{2\mathbf{y} - (R_{\max} + R_{\min})}{(R_{\max} - R_{\min})} \tag{26}$$

in which $\mathbf{y}$ is the actual value of a parameter for calibration and $R_{\max}$ and $R_{\min}$ represent the range of the parameter. Based on the underlying surface characteristics and the results of previous studies (Högström, 1996; Oleson et al., 2010), the ranges of the parameters to be calibrated are shown in Table 2. Then the turbulent flux parameterization schemes and the PSO algorithm is combined, and the surface layer turbulent related parameters are calibrated. The detailed realization method is depicted in the following flow chart (Fig. 2).

To evaluate the calibration and validation processes, the following expressions were proposed:

$$\text{Root mean bias error (RMBE)}: \ RMBE = \left(\sum_{i=1}^{N}(O_i - S_i)^2/\mathrm{N}\right)^{1/2} \tag{27}$$

$$\text{Mean bias error (MBE)}: \ MBE = \sum_{i=1}^{N}(O_i - S_i)/N \tag{28}$$

In the above expressions, O_i is the observation value, S_i the calculation value, N the number of samples. RMBE is a measure of the squared difference between the calculated and the measured values, whereas MBE is an indicator of the bias in the calculated values compared to the observations.

4. Results

Fig. 3 shows a comparison of the sensible heat flux calculated using the calibrated parameters for the C1 period and measurements with eddy correlation method. As shown in Fig. 3, the calculation reflected changes in the sensible heat flux rather well, which was consistent with the measurements. The scatterplot of the sensible heat flux (Fig. 4) showed that the linear fit line between the calculation and measurements was close to the 1:1 line, with a correlation coefficient greater than 0.90. Table 3 shows the averages of the calculations for each month in the C1 and C2 periods and the average, linear regression coefficient, intercept, correlation coefficient, error and KGE value of the measurements. As shown in Table 3, the averages of the calculated and measured values were very close, and the slope of their linear fit line was close to the 1:1 line with correlation coefficient greater than 0.9 and low mean error and root mean square error. A student t-test was run to test the mean values and correlation coefficients in every month, all passed the confidence of 95%. It implied that the differences in sensible heat fluxes between the calculation that used the calibrated parameters and the measurement were rather small and their correlation coefficients were relatively high.

As shown in Fig. 3, in the V1 period, the calculated heat fluxes were also consistent with the measurements, which suggested that the calibrated parameters had the temporal transferability to evaluate the sensible heat fluxes in this region. But as shown in Fig. 4 and Table 3, the bias between the calculated fluxes and measurements in the V1 period were larger than the C1 period. Fig. 5 shows the diurnal variations of sensible heat flux MBE in C1 and V1 period. As shown in Fig. 5, both of the highest errors occured close to noon. In C1 period, the maximum MBE is about 25 W m^{-2}, while in V1 period, the maximum MBE can up to 50 W m^{-2}. These results suggested that when the calibrated parameters used outside the calibration period, the bias increased.

Figs. 6 and 7 show a comparison of the calculated and measured momentum fluxes. Fig. 8 shows the diurnal variations of momentum flux MBE in C1 and V1 period. Table 4 shows numerous statistics for the calculated momentum flux. The pattern resembled that of the sensible heat flux. Furthermore, the global KGEs variation in C1 and C2 period was represented in Fig. 9 to better understand the calibration process. As show in Fig. 9, the global KGEs were converged after about 130 iterative times in every month, with all the values greater than 0.75.It implied that calibration process generated by the PSO algorithm and the MOST was rather stable and efficient.

In summary, the combination of the MOST and the PSO algorithm was able to simultaneously calibrate the turbulent flux parameters. The calibrated parameters enabled the fluxes of sensible heat and momentum fluxes to be reliably determined for different time periods. The calibration process was stable and efficient. In addition, this calibration process was neither limited to neutral conditions nor dependent on the profiles of the multi-layer wind velocity and potential temperature being very accurate as the conventional approach.

The variations of the calibrated parameters were depicted in Fig. 10. Table 5 lists the calibrated parameters during the C1 and C2 periods. As shown in Fig. 10, there were monthly variations in the calibrated parameters during the same calibration period. In addition, the calibrated parameters for a given month differed in the two periods. The empirical parameters did not exhibit any monthly trend, indicating a wide range of variations on a monthly scale. Therefore, the present similarity functions were not applicable to every month. Furthermore, the calculated annual mean values of β_m, β_h, γ_m and γ_h were 17.4, 14.1, 4.6 and 5.5 and 17.8, 15.6, 4.5 and 4.7 during the C1 and C2 periods, respectively. On an annual scale, the variations in these parameters were relatively

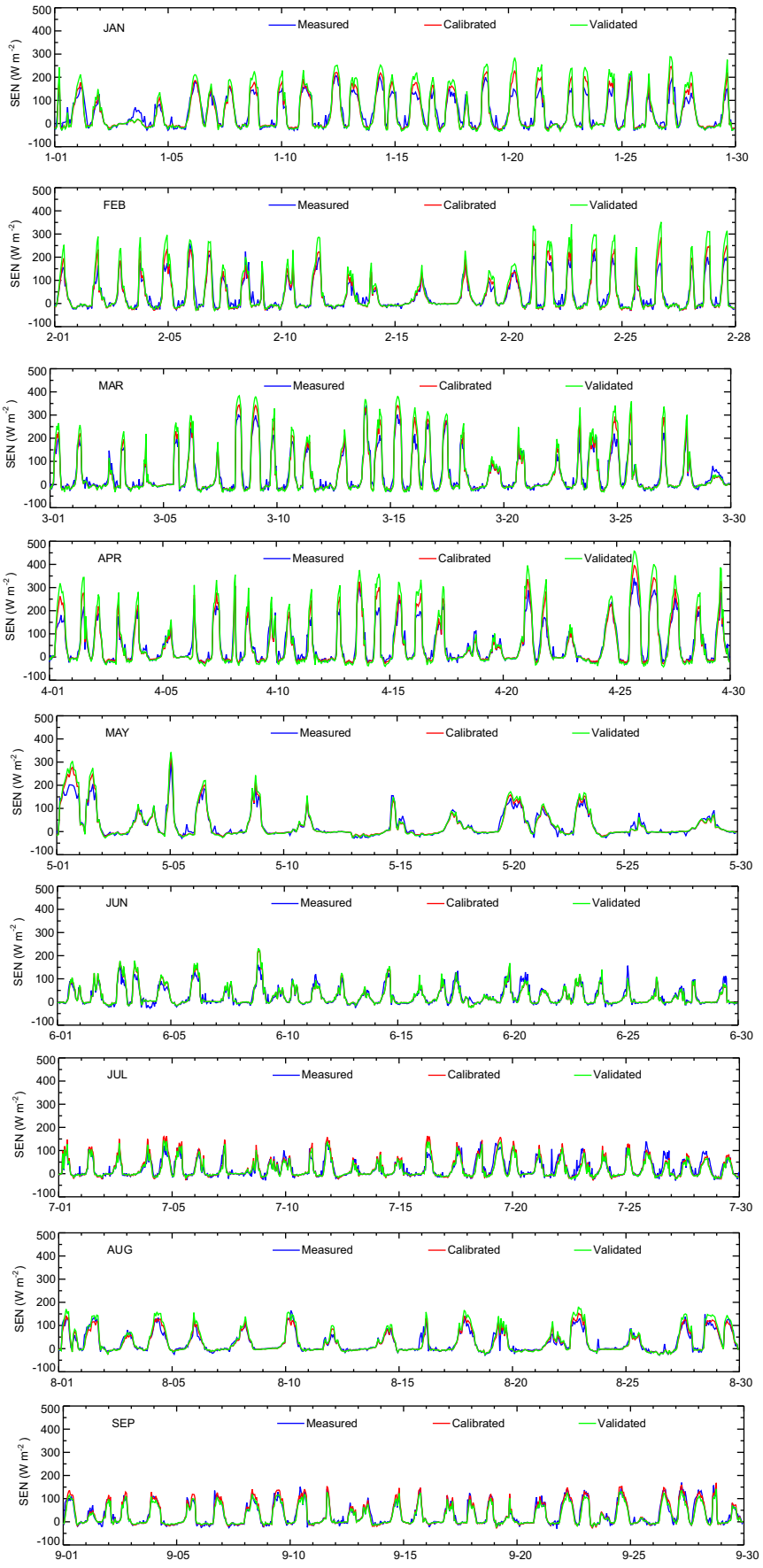

Fig. 3. Comparison of the calculated sensible (SEN) heat flux against measurement.

Table 2
The ranges of the parameters to be calibrated.

Variable	Symbol	Range
Momentum empirical parameters for stable	β_m	[2,8]
Sensible heat empirical parameters for stable	β_h	[2,8]
Momentum empirical parameters for unstable	γ_m	[10,30]
Sensible heat empirical parameters for unstable	γ_h	[10,30]
Aeroaerodynamic roughness	z_{0m}	[1e-4,1.0]
Parameter related with thermal and aeroaerodynamic roughness	Kb^{-1}	[0,20]

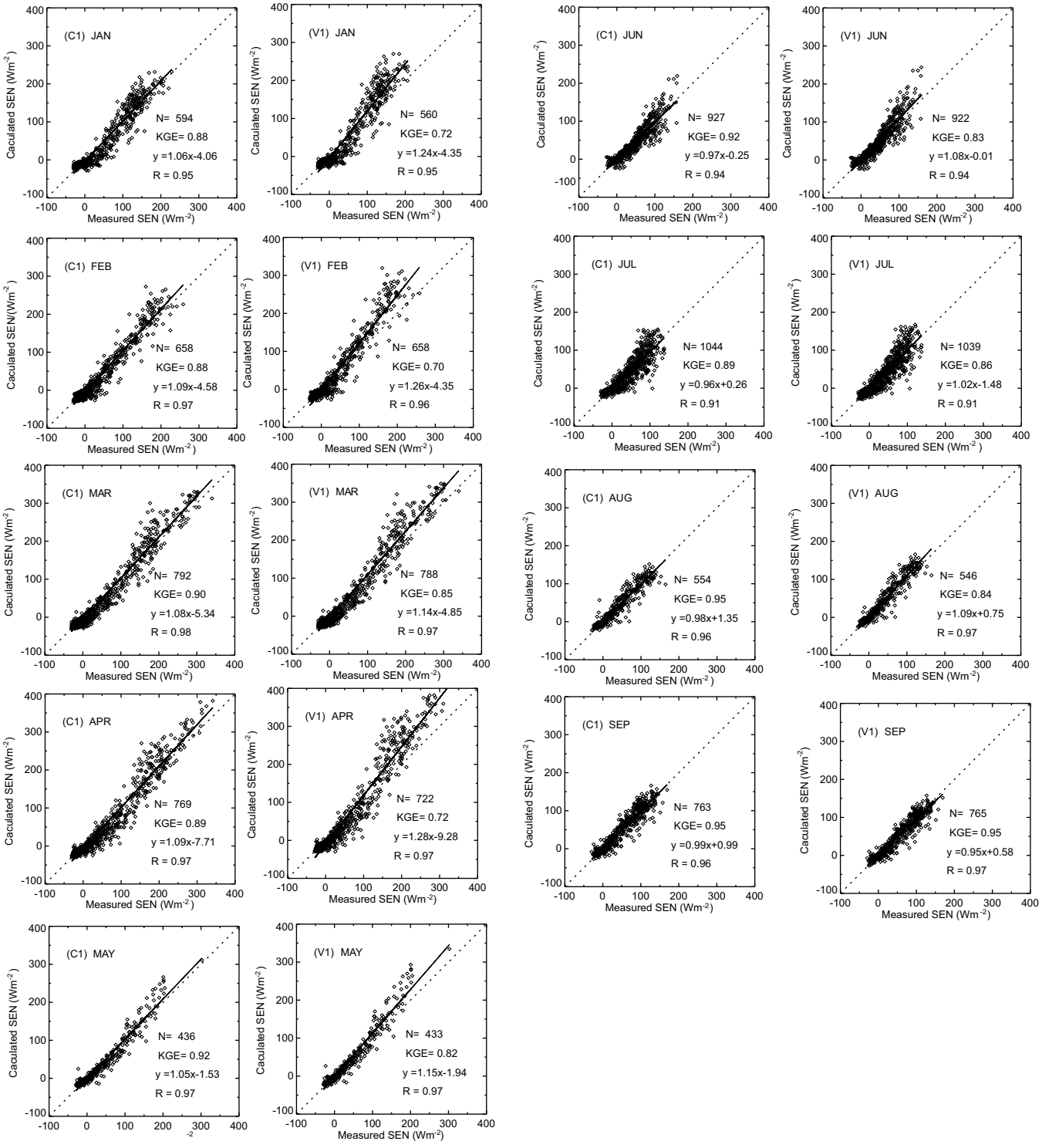

Fig. 4. Scatter plot of the sensible (SEN) heat flux calculation against measurement.

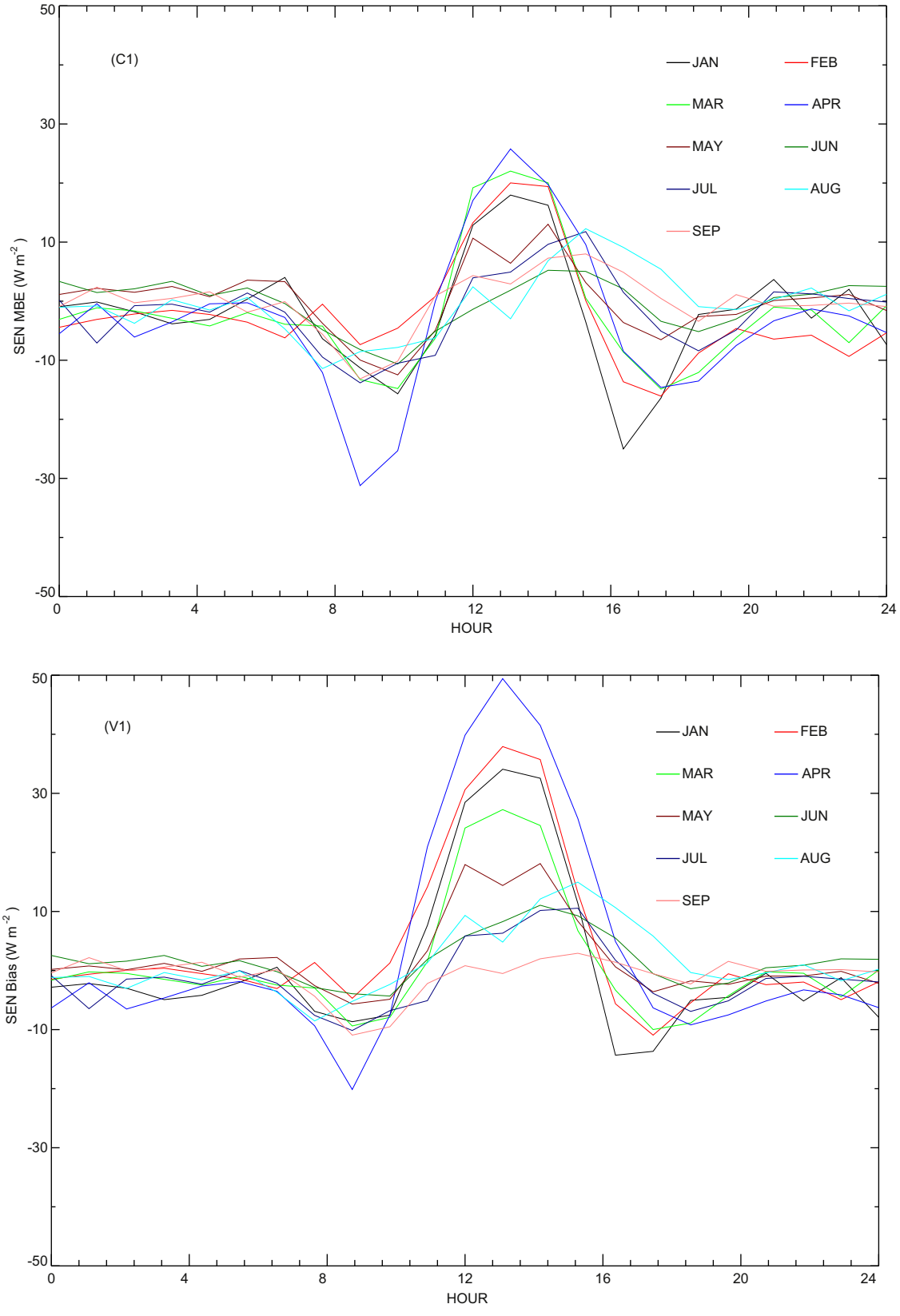

Fig. 5. The diurnal variations of sensible (SEN) heat flux MBE in C1 and V1 period.

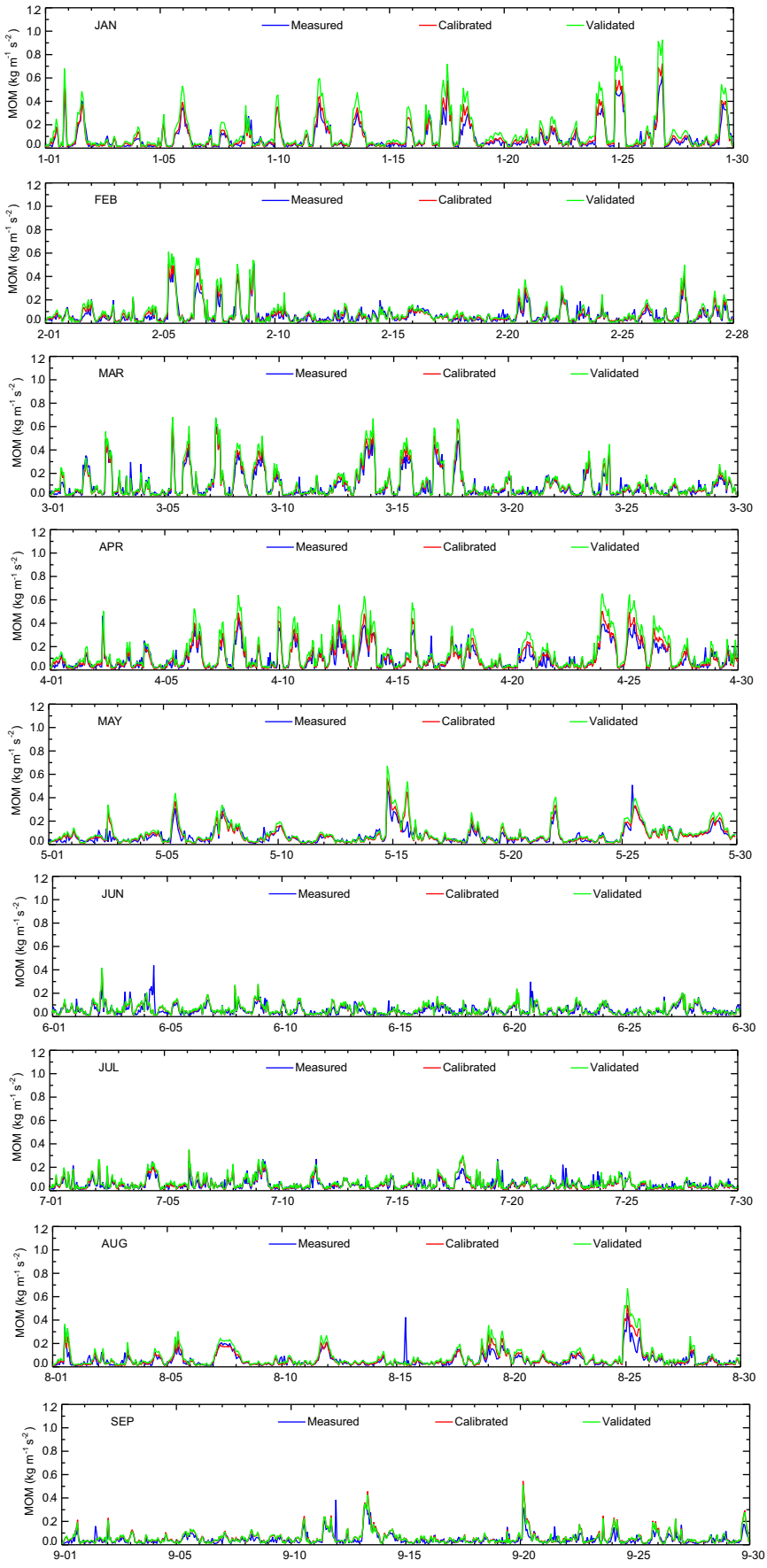

Fig. 6. Comparison of the calculated momentum (MOM) flux against measurement.

Table 3
Mean Values of the observed (Mean Obs) and calculated (Mean Cal) sensible heat flux; the Intercept, Slope, and R of the Linear Fit coefficients; and the RMSE, MBE and KGE value for different calibration and validation period (in brackets).

	Mean Obs	Mean Cal	Slope	Intercept	R	MBE	RMSE	KGE
JAN(C1/V1)	68.45	68.56 (73.46)	1.06 (1.24)	−4.06 (−4.35)	0.95 (0.95)	0.12 (10.82)	23.69 (34.34)	0.88 (0.72)
JAN(C2/V2)	39.11	36.04 (28.82)	1.05 (0.84)	−5.02 (−3.92)	0.92 (0.93)	−3.07 (−10.29)	27.88 (25.26)	0.83 (0.72)
FEB(C1/V1)	45.86	45.37 (60.50)	1.09 (1.26)	−4.58 (−4.35)	0.97 (0.96)	−0.49 (10.67)	19.82 (31.62)	0.88 (0.70)
FEB(C2/V2)	59.07	54.64 (43.86)	1.06 (0.91)	−8.12 (−9.69)	0.95 (0.95)	−4.42 (−15.21)	29.87 (28.71)	0.85 (0.65)
MAR(C1/V1)	57.67	56.72 (61.69)	1.08 (1.14)	−5.34 (−4.85)	0.98 (0.97)	−0.95 (3.19)	21.74 (25.52)	0.90 (0.85)
MAR(C2/V1)	65.03	60.70 (53.91)	1.04 (0.93)	−7.26 (−6.19)	0.95 (0.95)	−4.33 (−10.65)	32.01 (29.28)	0.87 (0.80)
APR(C1/V1)	68.56	66.94 (76.43)	1.09 (1.28)	−7.71 (−9.28)	0.97 (0.97)	−1.62 (9.66)	24.68 (39.09)	0.89 (0.72)
APR(C2/V2)	56.18	52.07 (59.17)	1.01 (1.18)	−4.72 (−7.17)	0.96 (0.96)	−4.11 (2.98)	23.22 (30.00)	0.90 (0.80)
MAY(C1/V1)	34.36	34.51 (35.52)	1.05 (1.15)	−1.53 (−1.94)	0.97 (0.97)	−0.15 (2.97)	14.79 (18.09)	0.92 (0.82)
MAY(C2/V2)	44.91	42.53 (42.02)	1.07 (1.05)	−5.44 (−4.95)	0.95 (0.95)	−2.38 (−2.89)	24.63 (24.11)	0.86 (0.86)
JUN(C1/V1)	29.15	28.18 (31.10)	0.97 (1.08)	−0.25 (−0.01)	0.94 (0.94)	−0.97 (2.39)	14.53 (16.47)	0.92 (0.83)
JUN(C2/V2)	34.39	33.28 (34.38)	0.98 (1.02)	−0.47 (−0.56)	0.95 (0.94)	−1.10 (−0.07)	16.21 (17.09)	0.93 (0.91)
JUL(C1/V1)	27.36	26.51 (25.40)	0.96 (1.02)	0.26 (−1.48)	0.91 (0.91)	−0.85 (−0.97)	17.07 (17.55)	0.89 (0.86)
JUL(C2/V2)	21.41	21.35 (20.82)	0.96 (0.94)	0.79 (0.68)	0.95 (0.95)	−0.06 (−0.59)	12.18 (12.37)	0.95 (0.94)
AUG(C1/V1)	31.58	32.37 (34.83)	0.98 (1.09)	1.35 (0.75)	0.96 (0.97)	0.79 (3.56)	12.52 (14.20)	0.95 (0.84)
AUG(C2/V2)	36.13	34.08 (29.87)	0.98 (0.86)	−1.19 (−1.26)	0.91 (0.90)	−2.05 (−6.26)	22.04 (21.81)	0.87 (0.76)
SEP(C1/V1)	36.74	37.33 (34.94)	0.99 (0.95)	0.99 (0.58)	0.96 (0.97)	0.59 (−1.21)	13.36 (12.47)	0.95 (0.95)
SEP(C2/V2)	43.18	40.27 (57.70)	1.00 (1.21)	−2.89 (−3.51)	0.90 (0.90)	−2.89 (4.52)	27.62 (29.39)	0.84 (0.75)

Table 4
Mean Values of the measurement and calculated momentum flux; the Intercept, Slope, and R of the Linear Fit coefficients; and the RMSE, MBE and KGE value for different calibration and validation period (in brackets).

	Mean Obs	Mean Cal	Slope	Intercept	R	MBE	RMSE	KGE
JAN(C1/V1)	0.084	0.086 (0.101)	1.03(1.32)	−0.001(0.001)	0.95(0.95)	0.002 (0.025)	0.034 (0.055)	0.89 (0.62)
JAN(C2/V2)	0.064	0.062(0.042)	0.94(0.71)	0.002(−0.003)	0.91(0.93)	−0.002 (−0.008)	0.038(0.042)	0.90(0.71)
FEB(C1/V1)	0.061	0.060 (0.072)	0.95(1.07)	0.002(0.001)	0.92(0.89)	−0.001 (0.005)	0.026(0.036)	0.91 (0.79)
FEB(C2/V2)	0.081	0.075(0.063)	1.03(0.87)	−0.008(−0.006)	0.93(0.95)	−0.006(−0.017)	0.041(0.037)	0.87(0.71)
MAR(C1/V1)	0.092	0.091 (0.097)	1.00(1.08)	−0.001(−0.004)	0.95(0.96)	−0.001 (0.004)	0.030(0.036)	0.94(0.87)
MAR(C2/V1)	0.106	0.101(0.085)	0.98(0.86)	−0.002(−0.005)	0.93(0.93)	−0.005(−0.019)	0.048(0.049)	0.90(0.75)
APR(C1/V1)	0.094	0.095 (0.117)	1.04(1.32)	−0.003(−0.004)	0.95(0.95)	0.001 (0.025)	0.030(0.054)	0.90(0.64)
APR(C2/V2)	0.078	0.071(0.054)	0.88(0.78)	0.010(0.005)	0.81(0.81)	−0.007(−0.024)	0.051(0.056)	0.78(0.63)
MAY(C1/V1)	0.073	0.075 (0.085)	1.06(1.19)	−0.001(0.001)	0.87(0.88)	0.002 (0.014)	0.036 (0.042)	0.78 (0.67)
MAY(C2/V2)	0.084	0.079(0.071)	0.84(0.83)	0.019(0.018)	0.79(0.79)	−0.006(−0.003)	0.064(0.063)	0.79(0.73)
JUN(C1/V1)	0.054	0.065 (0.064)	0.84(0.82)	0.019(0.019)	0.81(0.81)	0.011 (0.009)	0.036 (0.035)	0.75 (0.73)
JUN(C2/V2)	0.067	0.067(0.075)	0.80(0.86)	0.019(0.024)	0.81(0.79)	−0.006(0.007)	0.049(0.054)	0.71(0.66)
JUL(C1/V1)	0.054	0.055(0.079)	0.94(1.25)	0.004(0.009)	0.85(0.85)	0.001 (0.008)	0.024 (0.026)	0.83 (0.77)
JUL(C2/V2)	0.081	0.089(0.067)	0.85(0.81)	0.005(0.004)	0.82(0.85)	0.008(−0.013)	0.066(0.062)	0.79(0.70)
AUG(C1/V1)	0.058	0.063 (0.074)	1.11(1.14)	−0.002(−0.003)	0.92(0.92)	−0.005 (0.016)	0.027 (0.041)	0.80 (0.70)
AUG(C2/V2)	0.047	0.045(0.036)	0.83(0.81)	0.011(0.007)	0.83(0.81)	−0.002(−0.011)	0.041(0.039)	0.70(0.74)
SEP(C1/V1)	0.049	0.062 (0.064)	1.11(1.21)	0.004(0.011)	0.84(0.83)	0.014 (0.016)	0.040 (0.038)	0.78 (0.71)
SEP(C2/V2)	0.059	0.058(0.069)	0.81(0.80)	0.016(0.021)	0.90(0.89)	−0.001(0.009)	0.048(0.054)	0.70(0.63)

Table 5
Values of Calibrated parameters relating to the monthly turbulent flux.

	$\beta_{m,}$	β_h	γ_m	γ_h	z_{0m} (cm)	Kb^{-1}
JAN(C1)	17.49	14.56	6.58	5.62	0.93	5.41
JAN(C2)	20.05	17.80	6.02	3.71	1.84	6.66
FEB(C1)	16.16	11.09	3.37	3.89	0.73	6.87
FEB(C2)	21.19	19.83	6.31	6.32	1.13	6.60
MAR(C1)	17.09	12.89	3.74	6.36	0.59	7.48
MAR(C2)	18.59	12.90	3.65	4.71	0.86	6.30
APR(C1)	13.07	10.09	4.21	6.23	0.61	6.50
APR(C2)	10.58	10.21	2.50	4.77	1.41	7.46
MAY(C1)	16.18	15.41	3.04	5.66	0.77	6.96
MAY(C2)	11.17	10.96	3.14	3.50	1.41	7.49
JUN(C1)	17.80	17.33	5.69	5.96	1.22	6.12
JUN(C2)	19.28	19.14	4.90	5.79	1.31	6.37
JUL(C1)	15.40	12.86	4.06	5.53	2.82	1.81
JUL(C2)	16.98	15.84	2.59	4.19	3.10	4.34
AUG(C1)	23.93	19.53	5.27	4.81	2.04	1.44
AUG(C2)	21.21	18.90	5.53	5.28	3.89	2.10
SEP(C1)	19.40	13.28	5.74	5.31	3.16	2.22
SEP(C2)	20.99	14.93	5.43	4.14	2.66	3.76

small. The characteristic variations in z_{0m} were consistent during the C1 and C2 periods, with a minimum in March and a maximum in August (C1) or September (C2). The characteristic variations in Kb^{-1} were also consistent in periods C1 and C2, with higher values between January and June and lower values between July and September. But as shown in Table 5, the values of z_{0m} and Kb^{-1} were different in C1 and C2 periods, which implied that the difference would affect the validation process and result in the deviations. To decrease the deviation, several years' data should be employed to

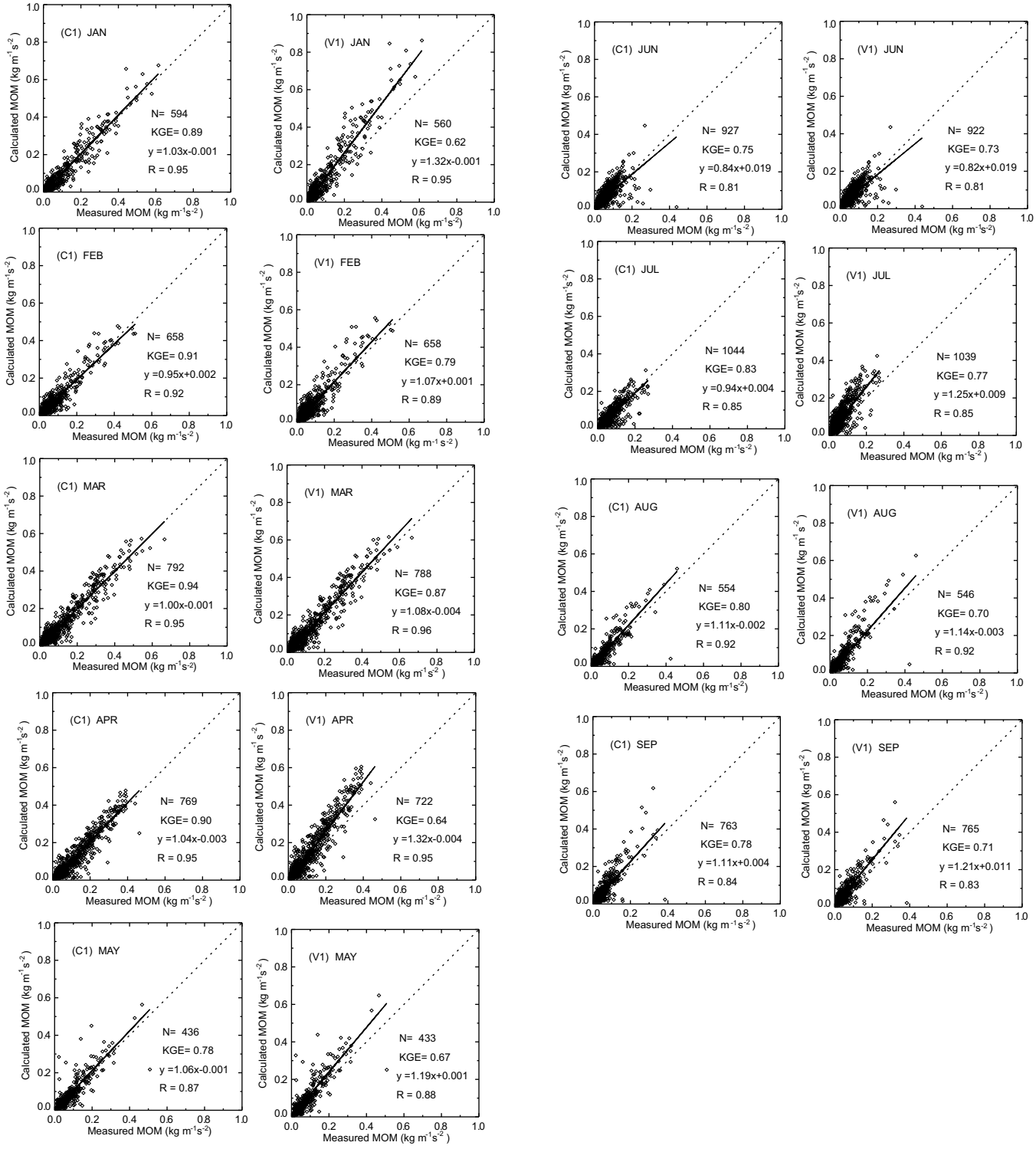

Fig. 7. Scatter plot of the momentum (MOM) flux calculation against measurement.

calibrate parameters and the mean value may be more suitable for numerical modeling.

5. Conclusions and discussions

Land-atmosphere exchanges of mass and energy determine the fundamental characteristics of a regional climate. Therefore, to understand regional climates and hydrological cycles, it is important to determine the parameters that relate to the turbulent flux in the surface layer and to develop optimal turbulent flux parameterization schemes using near-surface synthesis measurements. In numerical modeling, the turbulent flux parameterization is generally based on MOST. According to this theory, it is necessary to simultaneously determine the empirical similarity parameters β_m, β_h, γ_m and γ_h, the aerodynamic roughness (z_{0m}) and the thermal roughness (z_T). However, it is difficult to determine these six

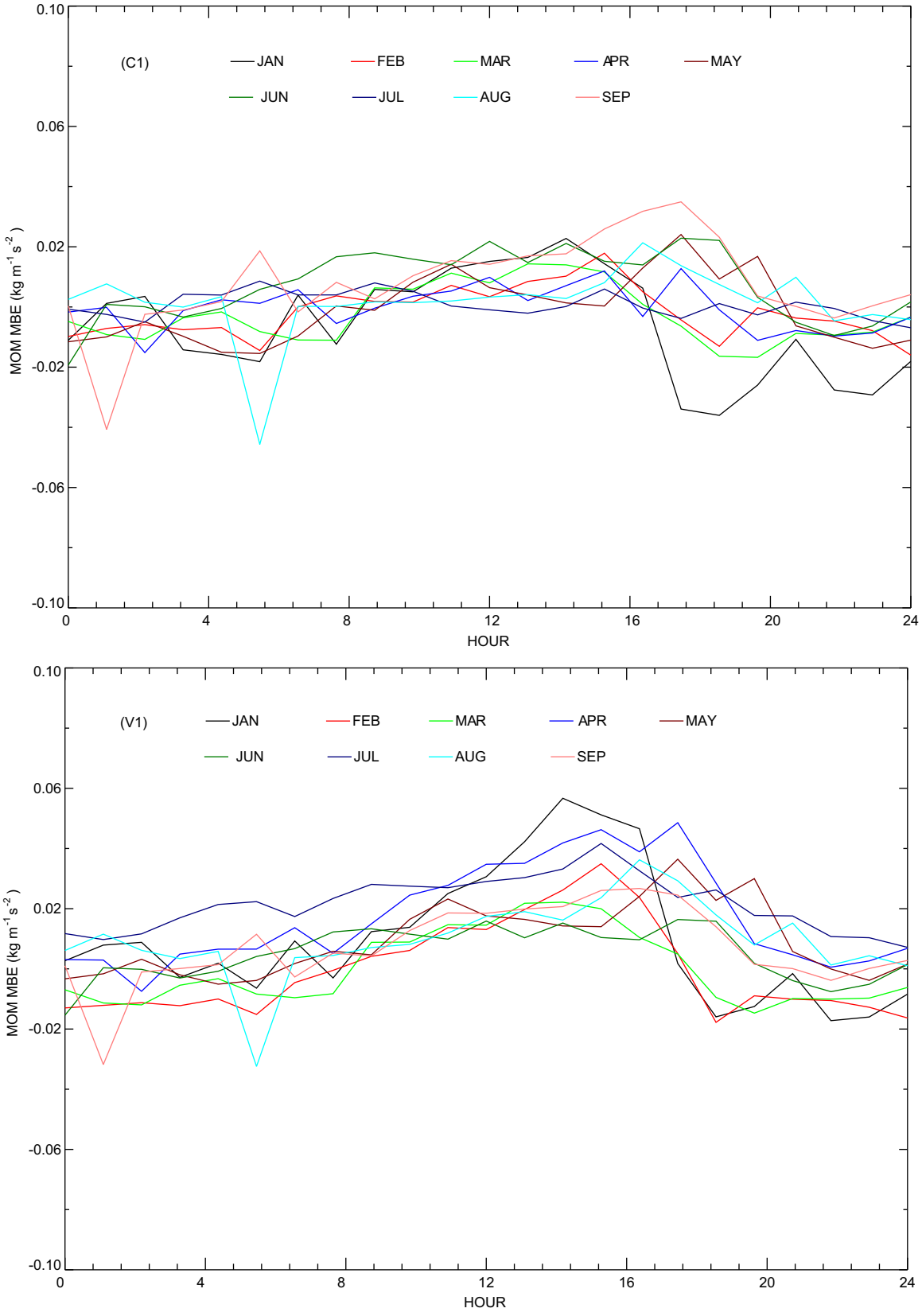

Fig. 8. The diurnal variations of momentum (MOM) flux MBE in C1 and V1 period.

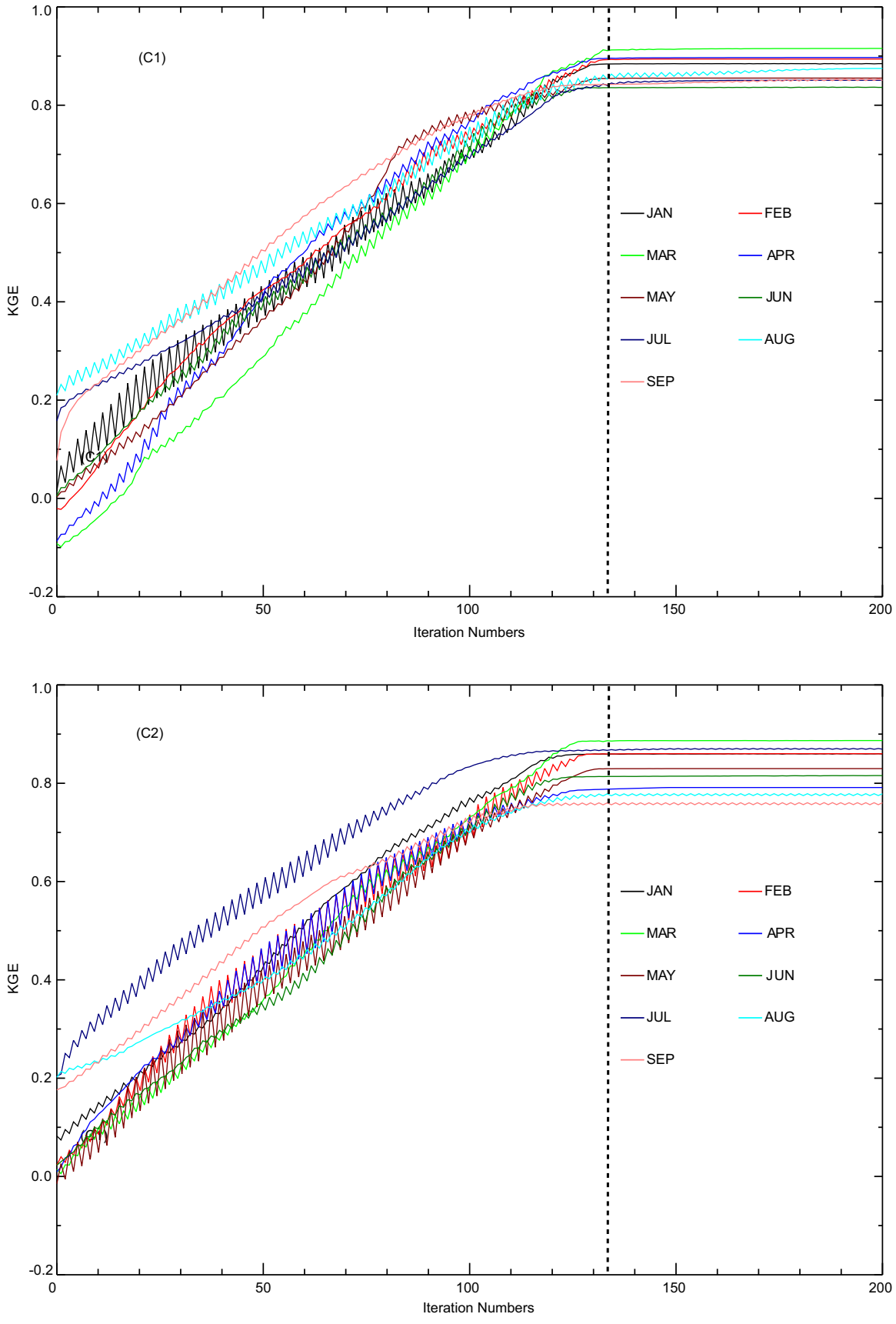

Fig. 9. The global KGEs variation in C1 and C2 period.

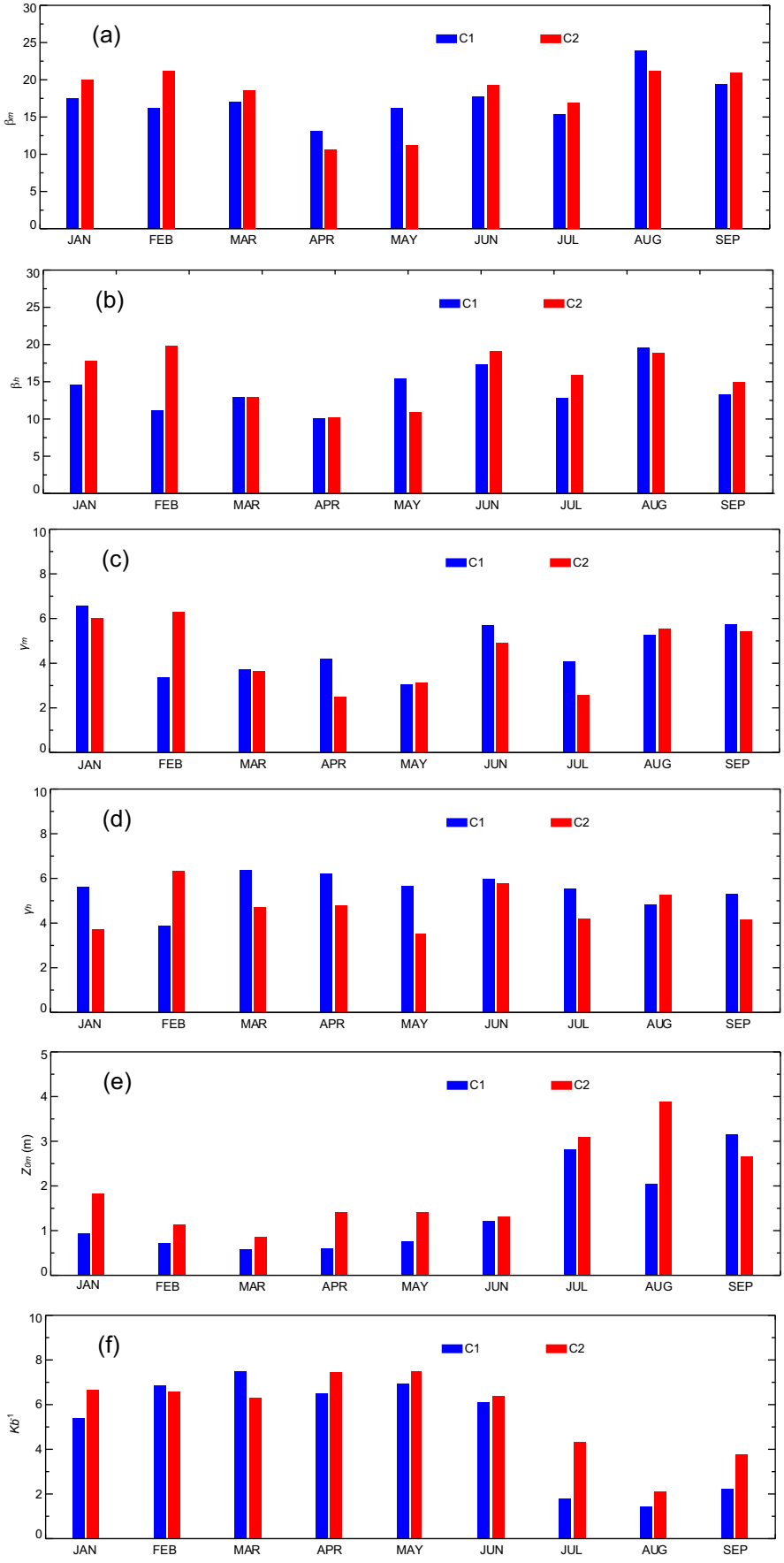

Fig. 10. The variations of the calibrated parameters during the C1 and C2 periods.

parameters simultaneously by solving a set of nonlinear equations. The artificial intelligence algorithm provides a feasible approach to solving this problem. With measurements from Maqu Station as a basis, this study used the PSO algorithm to calibrate the parameters relating to the monthly turbulent flux at the surface and calculated the fluxes of sensible heat and momentum using the calibrated parameters. This study concluded the following:

(1) Using the PSO algorithm, the surface layer turbulent flux parameters can be calibrated simultaneously. The fluxes of sensible heat and momentum calculated with the calibrated parameters using MOST were close and highly correlated to the measured values; their linear fit lines had slopes of nearly one.
(2) The calibrated empirical similarity parameters showed monthly variations that did not have any trend, which suggested that there is a wide range of monthly variation in these empirical parameters, and the present similarity functions may not be fully applicable to every month. The characteristic variations in z_{0m} and Kb^{-1} were consistent while the values were different in two calibration periods. Therefore, deviations may be introduced when these parameters transferred outside the calibration periods.

Our study showed that the PSO algorithm can be used to calibrate the parameters relating to turbulent flux in the surface layer. There still exist a few problems in using the PSO algorithm or other optimization algorithms, which must be addressed in future studies, as follows: (1) Parameters obtained by an optimization algorithm should be further tested against observations. In fact, the surface layer parameters or parameter combinations calibrated by the PSO algorithm are only optimal solutions of MOST equations. These solutions have no specific physical meanings. How to combine the optimal solution with the actual physical process required to further proved; (2) As a major drawback of the PSO algorithm, a number of parameters inherent to algorithm have to be determined, though these parameters have no effect on the optimal solution. Like other optimization algorithms, if a multi-objective function is defined in the PSO algorithm, we can only obtain the Pareto solution of the problem; (3) The number of calibration parameters should be limited. Because each parameter can be selected within its range. With the number of calibration parameters increased, the corresponding combinations for the parameters were also increased. However, Finding the optimal solution would be more difficult within finite times and iterations. In summary, it is of equal importance to conduct comprehensive near-surface observational experiments, and combine optimization algorithms to accurately identify surface layer parameters or parameter combinations, which can eventually improve the accuracy of turbulent fluxes between atmosphere and land surface.

Acknowledgments

This work is supported by the R&D Special Fund for Public Welfare Industry (GYHY201406001), Natural Science Foundation of China (41305103 and 41275162) and Yunnan Province (2013FD005), and the Jiangsu Collaborative Innovation Center for Climate Change. We also thank the Maqu station for providing the observation data and High Performance Computing Center of Yunnan University for computational support.

References

Abdella, K., McFarlane, N.A., 1996. Parameterization of the surface-layer exchange coefficients for atmospheric models. Boundary-Layer Meteorol. 80 (3), 223–248.
Beljaars, A.C.M., Holtslag, A.A.M., 1991. Flux parameterization over land surfaces for atmospheric models. J. Appl. Meteorol. 30 (3), 327–341.
Businger, J.A., Wyngaard, J.C., Izumi, Y., Bradley, E.F., 1971. Flux-profile relationships in the atmospheric surface layer. J. Atmos. Sci. 28 (2), 181–189.
Chau, K.W., 2006. Particle swarm optimization training algorithm for ANNs in stage prediction of Shing Mun River. J. Hydrol. 329 (3–4), 363–367.
Chen, F., Janjić, Z., Mitchell, K., 1997. Impact of atmospheric surface-layer parameterizations in the new land-surface scheme of the NCEP mesoscale eta model. Boundary-Layer Meteorol. 85 (3), 391–421.
Crow, W.T., Wood, E.F., Pan, M., 2003. Multiobjective calibration of land surface model evapotranspiration predictions using streamflow observations and spaceborne surface radiometric temperature retrievals. J. Geophys. Res.: Atmos. 108 (D23), 4725.
Cuo, L., Zhang, Y., Gao, Y., Hao, Z., Cairang, L., 2013. The impacts of climate change and land cover/use transition on the hydrology in the upper Yellow River Basin, China. J. Hydrol. 502, 37–52.
Dai, Y., et al., 2003. The common land model. Bull. Am. Meteorol. Soc. 84 (8), 1013–1023.
Dickinson, R.E., Shaikh, M., Bryant, R., Graumlich, L., 1998. Interactive canopies for a climate model. J. Clim. 11 (11), 2823–2836.
Dyer, A.J., 1974. A review of flux-profile relationships. Boundary-Layer Meteorol. 7 (3), 363–372.
Fu, G., Chen, S., Liu, C., Shepard, D., 2004. Hydro-climatic trends of the yellow river basin for the last 50 years. Clim. Change 65 (1), 149–178.
Garratt, J.R., Pielke, R.A., 1989. On the sensitivity of mesoscale models to surface-layer parameterization constants. Boundary-Layer Meteorol. 48 (4), 377–387.
Gill, M.K., Kaheil, Y.H., Khalil, A., McKee, M., Bastidas, L., 2006. Multiobjective particle swarm optimization for parameter estimation in hydrology. Water Resour. Res. 42 (7), 257–271.
Gupta, H.V., Bastidas, L.A., Sorooshian, S., Shuttleworth, W.J., Yang, Z.L., 1999. Parameter estimation of a land surface scheme using multicriteria methods. J. Geophys. Res.: Atmos. 104 (D16), 19491–19503.
Gupta, H.V., Kling, H., Yilmaz, K.K., Martinez, G.F., 2009. Decomposition of the mean squared error and NSE performance criteria: implications for improving hydrological modelling. J. Hydrol. 377 (1–2), 80–91.
Högström, U., 1988. Non-dimensional wind and temperature profiles in the atmospheric surface layer: a re-evaluation. Boundary-Layer Meteorol. 42 (1), 55–78.
Högström, U., 1996. Review of some basic characteristics of the atmospheric surface layer. Boundary-Layer Meteorol. 78 (3), 215–246.
Hu, Y., Maskey, S., Uhlenbrook, S., 2012. Trends in temperature and rainfall extremes in the Yellow River source region, China. Clim. Change 110 (1), 403–429.
Kanda, M., Kanega, M., Kawai, T., Moriwaki, R., Sugawara, H., 2007. Roughness lengths for momentum and heat derived from outdoor urban scale models. J. Appl. Meteorol. Climatol. 46 (7), 1067–1079.
Kennedy, J., Eberhart, R., 1995. Particle swarm optimization. Proc. IEEE Int. Conf. Neural Networks 4, 1942–1948.
Łobocki, L., 1993. A procedure for the derivation of surface-layer bulk relationships from simplified second-order closure models. J. Appl. Meteorol. 32 (1), 126–138.
Louis, J.-F., 1979. A parametric model of vertical eddy fluxes in the atmosphere. Boundary-Layer Meteorol. 17 (2), 187–202.
MacKinnon, D.J., Clow, G.D., Tigges, R.K., Reynolds, R.L., Chavez Jr., P.S., 2004. Comparison of aerodynamically and model-derived roughness lengths (zo) over diverse surfaces, central Mojave Desert, California, USA. Geomorphology 63 (1–2), 103–113.
Monin, A.S., Obukhov, A.M., 1954. Basic laws of turbulent mixing in the surface layerof the atmosphere. Tr. Akad. Nauk SSSR Geophiz. Inst. 24 (151), 163–187.
Niu, G.-Y., et al., 2011. The community Noah land surface model with multiparameterization options (Noah-MP): 1. Model description and evaluation with local-scale measurements. J. Geophys. Res.: Atmos. 116 (D12), 1248–1256.
Oleson, K.W. et al. 2010. Technical Description of version 4.0 of the Community Land Model (CLM). NCAR Technical Note NCAR/TN-478+STR.
Paulson, C.A., 1970. The mathematical representation of wind speed and temperature profiles in the unstable atmospheric surface layer. J. Appl. Meteorol. 9 (6), 857–861.
Poli, R., Kennedy, J., Blackwell, T., 2007. Particle swarm optimization. Swarm Intell. 1 (1), 33–57.
Scheerlinck, K., Pauwels, V.R.N., Vernieuwe, H., De Baets, B., 2009. Calibration of a water and energy balance model: recursive parameter estimation versus particle swarm optimization. Water Resour. Res. 45 (10), W10422.
Schmitt, M., Wanka, R., 2015. Particle swarm optimization almost surely finds local optima. Theor. Computer Sci. 561, 57–72, Part A.
Seneviratne, S.I., Luthi, D., Litschi, M., Schar, C., 2006. Land-atmosphere coupling and climate change in Europe. Nature 443 (7108), 205–209.
Sharan, M., Srivastava, P., 2014. A semi-analytical approach for parametrization of the obukhov stability parameter in the unstable atmospheric surface layer. Boundary-Layer Meteorol. 153 (2), 339–353.
Sorbjan, Z., 1986. On similarity in the atmospheric boundary layer. Boundary-Layer Meteorol. 34 (4), 377–397.
Sun, J., 1999. Diurnal variations of thermal roughness height over a grassland. Boundary-Layer Meteorol. 92 (3), 407–427.

Yang, K., Tamai, N., Koike, T., 2001. Analytical solution of surface layer similarity equations. J. Appl. Meteorol. 40 (9), 1647–1653.
Yang, K., Koike, T., Yang, D., 2003. Surface flux parameterization in the Tibetan plateau. Boundary-Layer Meteorol. 106 (2), 245–262.
Yang, K., et al., 2008. Turbulent flux transfer over bare-soil surfaces: characteristics and parameterization. J. Appl. Meteorol. Climatol. 47 (1), 276–290.
van den Hurk, B.J.J.M., Holtslag, A.A.M., 1997. On the bulk parameterization of surface fluxes for various conditions and parameter ranges. Boundary-Layer Meteorol. 82 (1), 119–133.
Zeng, X., Dickinson, R.E., 1998. Effect of surface sublayer on surface skin temperature and fluxes. J. Clim. 11 (4), 537–550.